Arabian Journal of Chemistry (2022) **15**, 103949

King Saud University

Arabian Journal of Chemistry

www.ksu.edu.sa
www.sciencedirect.com

ORIGINAL ARTICLE

An innovative SiO_2-pyrazole nanocomposite for Zn(II) and Cr(III) ions effective adsorption and anti-sulfate-reducing bacteria from the produced oilfield water

Rasha A El-Saeed [a], R. Hosny [b], Mahmoud F. Mubarak [b], Moaz M. Abdou [b,*], Kamel R. Shoueir [c,d]

[a] *Department of Chemistry, Faculty of Science, Mansoura University, ET-35516 Mansoura, Egypt*
[b] *Egyptian Petroleum Research Institute, Nasr City, 11727 Cairo, Egypt*
[c] *Institute of Nanoscience & Nanotechnology, Kafrelsheikh University, 33516 Kafrelsheikh, Egypt*
[d] *Institut de Chimie et Procédés pour l'Énergie, l'Environnement et la Santé (ICPEES), CNRS UMR 7515-Université de Strasbourg, 25 rue Becquerel, 67087 Strasbourg, France*

Received 27 January 2022; accepted 4 May 2022
Available online 16 May 2022

KEYWORDS

Pyrazoles;
Mesopores silica;
Produced oilfield water;
Adsorption;
Zn(II) and Cr(III) ions, SRB

Abstract Novel SiO_2-pyrazole (**SiO_2-PYZ**) nanocomposite was introduced for the elimination of Zn(II) and Cr(III) from oil reservoir water. Characterization analysis of prepared **SiO_2-PYZ** nanocomposite was investigated using SEM, FTIR, TGA, XRD, TEM, and BET. Studying the effects and optimization of the parameters such as retention time, pH, initial Cr(III) and Zn(II) ions concentrations, adsorbent dosage, and temperature were examined. For kinetics investigation, the pseudo-second-order (PSO) model matches the adsorption process effectively under different operating conditions. After applying two other isotherm models (Langmuir and Freundlich), the experimental data was adequately equipped with Langmuir, $R^2 = 1$. The thermodynamic results pointed that the adsorption of Zn(II) and Cr(III) ions was spontaneous, endothermic, and physisorption reaction. At pH 12, the influence of more than one ion, such as Ca(II) and Na(I), was checked, and the results revealed that this conjugate substance was highly selective to Cr(III). After washing

* Corresponding author.
E-mail address: moaz.chem@gmail.com (M.M. Abdou).
Peer review under responsibility of King Saud University.

Production and hosting by Elsevier

https://doi.org/10.1016/j.arabjc.2022.103949

with water in multiple cycles, the adsorbed material was regenerated with 0.1 M HCl and subsequently reused without deterioration in its case cavities. Interestingly, **SiO_2-PYZ** was highly effective against sulfate-reducing bacteria (SRB) in the petroleum field.

1. Introduction

The significant problem of the oil production process was the produced water loaded with many corrosive salts and contained sulfate-reducing bacteria (SRB). These bacteria release hydrogen sulfide and materials' potential related odor and corrosion (Ortenberg, 2003). Moreover, this produced water interacts with the internal production lines of wells, leading to samples of elements such as zinc (Zn(II)) and chromium (Cr(III)) in the water (Fathy, 2018; Fathy, 2015; El-Maghrabi, 2018). These elements are more sensitive to the marine environment upon discharge into the surface water (Wang et al., 2022; Aldawsari, 2020; Aldawsari, 2021; Aldawsari, 2021).

Over 170 thousand tons of chromium-containing waste are estimated to be discharged into the aquatic system and the environment each year by various industrial processes, including pharmacology, electroplating, tanning metallurgy, and battery manufacturing. Zn(II) and Cr(III) tend to stay in the human body over time, consequently increasing the chemical concentrations in biological organisms (Mubarak and Hosny, 2021). However, Cr(III) is less hazardous than hexavalent chromium [Cr(VI)] (Wang, 2017; Bakshi and Panigrahi, 2018; Mubarak, 2021; Ali, 2021; Shoueir, 2020); an excessive amount of chromium posing a severe problem led to lung cancer and many disorders in the liver and kidney (Proctor, 2014; Beveridge, 2010). This ion can cause skin irritations such as rashes, ulcers, and permanent scarring upon direct contact with skin. On the other hand, Zn ions are more toxic and lead to intense pollutants (Vardhan et al., 2019).

Before the wastewater discharges into the environment, treating metal-contaminated wastewater is essential to reduce toxicity. Even though the traditional techniques are often chemically, energetically, and operationally intensive (Shoueir, 2016; El-Kemary, 2018; Shoueir, 2017; Shoueir, 2016).

Previously discussed, conventional heavy metal elimination strategies from wastewater include flocculation, coagulation, electrochemical, ozonation, and biological treatment (Barakat, 2011). High inputs, hazardous byproducts, and inadequate metal removal techniques are only a few of the drawbacks of such methods. In recent decades, technologies for removing low trace metals from wastewater and water supplies have been developed that are both less expensive and more successful (Bailey, 1999).

These are typically interested in using small systems that provide technological hurdles during implementation and operation on a large scale (Basu, 2019). As a result, scientists have spent a lot of time developing new methods (Owlad, 2009; Hosny, 2019). Recently, adsorption technology has gotten a lot of attention because of its high efficiency, selectivity, flexibility in use, and being economically feasible and affordable in practical applications (Fu and Wang, 2011; Kausar, 2018; Kausar, 2017; Naeem, 2017).

It has been important for analytic and environmental applications to prepare silica-based adsorbents for water remediation. An efficient adsorbing matrix should be a stable, insoluble porous matrix with appropriate active groups that interact easily with the analyte (El-Maghrabi, 2019). Given its surface reactivity and capacity to trap organic molecules on the surface, silica gel is considered strong support for organic groups (the inorganic material that does not swell and remains stable in acidic environments). Besides, the organo-functional silicas are resistant to organic solvents or water removing the ligand from the surface and having good thermal resistance (Massie, 1980).

Structural mesopores silica nanoparticles piqued more interest because of their surface characteristics which paved research towards vital applications such as environmental protection, sensing applications, biomedical, catalysis, and elimination of toxins such as heavy metals, organic pollutants, and persistent contaminants (Da'na, 2017). Mesoporous silica gained more attention because of its appropriate surface modification, well-defined pores, and geometrical pore structure. SBA-15, MCM-41, and HMS are categorized under the potent mesoporous materials and have been functionalized to be used in the literature to remove traces of hazardous metals from polluted waters (Kong et al., 2021).

The silica-based adsorbent was used as a convenient method for capturing heavy-metal ion contaminants from wastewaters (Rahman and Nasir, 2020; Rahman, 2021). A functionalized bipyrazole was condensed with a 3-glycidoxy propyl-trimethoxysilane silylant agent (SG2P) to produce a pure adsorbent based hybrid polymer, previously anchored on a silica surface, which demonstrates a high degree of selectivity against Hg^{2+} ion (Radi, 2015).

The use of pyrazoline as a coating material for silica nanoparticles such as **MCM-41** is one of the rare applications and techniques in core–shell processing. According to some studies, the core–shell system is always intended to use a solid surface and core, typically a metallic or polymeric structure. Due to the initial findings and our long-term chemistry program of 1,3-diketones and their various utilization (Abdou, 2019; Abdou, 2019; Abdou, 2017; Abdou, 2016; Abdou, 2017; El-Mahalawy et al., 2021; Abdou, 2017; Abdou, 2018; El-Mahalawy et al., 2022). Herein, chemical bonding between the thin layer of pyrazoline on the silica surface acts as a coating shell that allows for various chemical surface properties to be achieved. The use of this type of complex in water treatment will enhance the economic operation of any treatment system and add to the core–shell category as a new group of complexes with an amorphous organic thin film. The essential aims of this paper are to prepare **SiO_2-PYZ** nanocomposite as a strong adsorbent for the elimination of Zn(II) and Cr(III). Characterization tools of **SiO_2-PYZ** were performed using SEM, FTIR, TGA, XRD, TEM, and BET. The kinetics, isotherm, and thermodynamics are all being investigated. The

adsorption mechanism based on controlled pH was also discussed.

2. Experiments

2.1. Materials and techniques

The working solutions of metal ions were prepared from zinc nitrate hexahydrate (Merck, purity > 99%) and chromic(III) nitrate non-hydrate. Calcium chloride ($CaCl_2 \cdot 4H_2O$), sodium chloride (NaCl), cetyltrimethylammonium bromide(CTAB) (Carlo Erba, 99% purity), tetraethyl orthosilicate (TEOS) were purchased from MERCK company. The functional moieties on the surface adsorbent (mesoporous silica and **SiO_2-PYZ**) were analyzed using FTIR in the presence KBr (Thermo Scientific, USA). A TGA (SDT Q600 V5.0 Build 63 (TA, America) was carried out to evaluate the thermal stability, starting from room temperature to 800 °C. The mineralogical composition and the crystalline structures of the mesoporous silica and **SiO_2-PYZ** were analyzed *via* XRD (D8 ADVANCE, Bruker, Germany). SEM was carried out using (EVO 10) with electron source tungsten filament. TEM observations (JEOL-JEM-1200 EX) were used to elucidate the designed nanoparticles' shape and size. For surface characteristics, BET was used to determine the surface features performed in automatic equipment (ChemBET 3000, Quantachrome). The concentrations of Zn (II) and Cr(III) were determined using an atomic absorption spectrometer, Analytic Jena (ZEEnit 700P, Germany).

2.2. Synthesis of organic pyrazoline ligand (PYZ)

The selected organic **PYZ** ligand was prepared according to our previous protocol (Metwally, 2012; Metwally, 2012; Metwally, 2013; Abdou, 2013).

2.3. Preparation of mesoporous silica by ultrasound methods

Mesoporous silica was prepared with the addition of TEOS to an aqueous solution containing CTAB, 2 M of NaOH, and deionized water using a modified conventional synthesis protocol (El-Maghrabi, 2018). For TEOS@CTAB@NaOH@H_2O, the molar composition was 1.0:0.09:3.57:62.05 to produce a gel mixture. The mixture pH was fixed at 9 by adding sulfuric acid after a further stirring with ultrasound irradiance (35 kHz) for 30 min at 35 °C. At room temperature (R.T), the mixture was maintained for one day. The resulting white powder was treated (filtered, washed, and dried at 70°C for one day). The samples were calcined in the open air at a rate of 1 °C per minute for 5 h at 550 °C to eliminate the template. The final material obtained was used for all further studies.

2.4. Synthesis of mesoporous silica-PYZ nanocomposite

Approximately 5.4 g of prepared mesoporous **MCM-41** was added to 50 ml acetone, and vigorous agitation lasted 30 min to prepare **SiO_2-PYZ**. The filtered solution was subsequently mixed with **PYZ** (0.05 g), and the final mixture was mixed for another 2 h at 100 °C in pure acetone until evaporation took place. For 24 h, the synthetic composite has been filtered and dried. Scheme 2 is a simplistic representation showing the synthetic pathway.

2.5. Adsorption of Zn(II) and Cr(III) by SiO_2-PYZ

Different parameters that influence the removal efficiency using **SiO_2-PYZ** were studied inside the cupboard and in the presence of an incubated shaker. The impact of pH, retention time, and adsorbent dosage was investigated. By taking all other parameters constant, the dose ranged from 0.05 to 1 g/l. To determine the pH influence of the first solutions, diluted concentrations from HCl and NaOH solutions were used for controlling pHs between 2 and 12. The retention time was changed from 5 to 120 min. After reaching the predetermined time, filtration is required to separate the adsorbent. The experiments were also conducted at different ions concentrations (50–500 mg/l) to attain equilibrium adsorption isotherm. The concentrations of Zn(II) and Cr(III) in solution were determined using atomic absorption spectrometry. Concentration was measured at least three times, and the result was their average. A cellulose membrane was utilized to filtrate the solution after adsorption's Zn(II) and Cr(III) adsorption performance (E %) is given by the following equations:

$$E\% = \left[\frac{(C_O - C_t)}{C_O}\right] \times 100 \quad (1)$$

Pollutant adsorption capacity is given by:

$$Q(mg/g) = \frac{C_O - C_t}{m} \quad (2)$$

C_o is the starting solution concentration before adsorption in mg/l, C_t is the solution ion concentration after adsorption (mg/l), and m (g) is the one-liter solution containing the mass

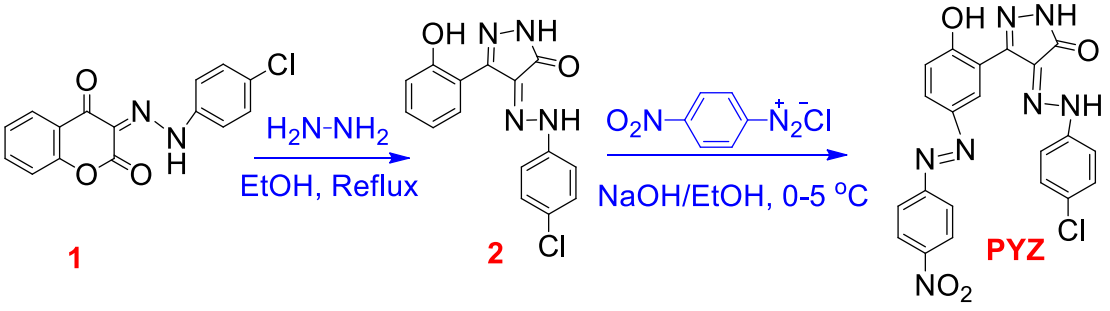

Scheme 1 The synthesis of **PYZ** ligand.

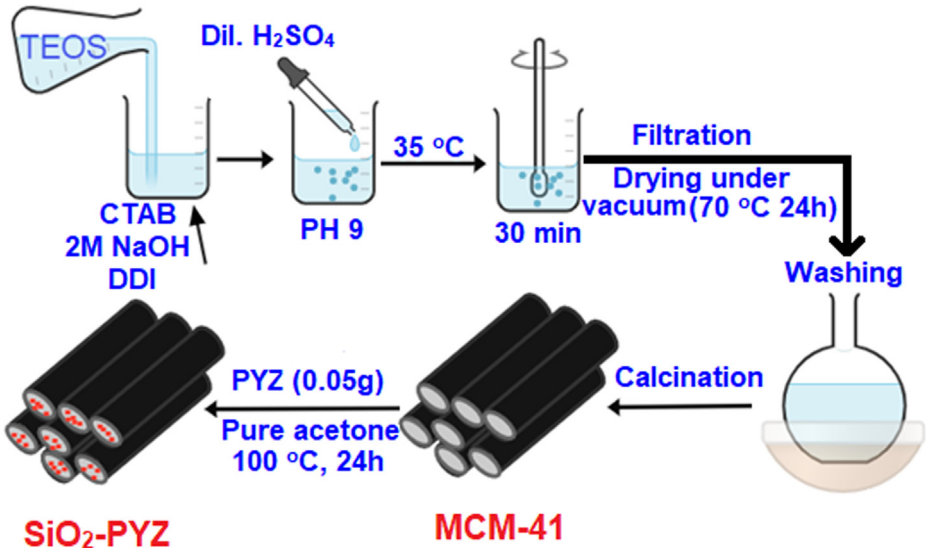

Scheme 2 Mechanistic synthesis of mesoporous silica **MCM-41** and **SiO_2-PYZ** nanocomposite.

adsorbent. A proper solvent is required to desorb the adsorbing substances for multi-use immediately after the batch adsorption process.

2.6. Reusability

The recyclability of the adsorbent is very important for its practical application. **SiO_2-PYZ** was evaluated through Zn (II) and Cr(III) adsorption/desorption cycles to test its recyclability. **SiO_2-PYZ** was immersed in a 10 ml aqueous solution of a single metal ion (500 mg/l). After each adsorption step, the **SiO_2-PYZ** sample was regenerated by stirring M(X)-loaded **SiO_2-PYZ** in 0.1 M HCl for one hour. After centrifugation and washing with distilled water, the samples were vacuum-dried at 50 °C for 30 min. Regenerated **SiO_2-PYZ** was then used for the next metal ion adsorption cycle, and this step as a regeneration procedure was repeated five times.

2.7. Microbial-induced corrosion evaluation study

After production, SRB-contaminated oil tank, water samples were collected from the bottom of the tank. Under the anaerobic circumstances provided by this position, this location is suitable for colonization growing SRBs (Wakai, et al., 2018; Wakai, 2020). In such situations, SRB can have strong MIC effects (Silva, 2020). The Egyptian Petroleum Research Institute (EPRI) procured specific media to quantitatively determine the growth rate of SRB bacteria, prepared according to NACE TM0194-14-SG (Sun et al., 2018) and sealed in insulated vials. The test procedure followed the NACE TM0194-14-SG standard test and our earlier research (Abbas, 2021).

3. Results and discussion

3.1. Synthesis of organic pyrazoline ligand (PYZ)

The synthetic approach for the organic synthesis of **PYZ** is shown in Scheme 1, as we previously published (Metwally, 2012; Metwally, 2012; Metwally, 2013; Abdou, 2013). Treatment of azo coumarin **1** (Abdou et al., 2019; Abdou et al., 2019; Metwally, 2012) with NH_2NH_2 in EtOH afforded the corresponding pyrazolinone **2**. Diazo coupling of **2** with diazotized 4-nitroaniline in basic solution yielded the target organic **PYZ** ligand.

3.2. Characterization

3.2.1. FTIR

The FTIR spectrum of organic silica material has similar features in the two samples. The Si-O stretching band and a range of 1240–1099 cm^{-1} were assigned to a fingerprint region of mesoporous **MCM-41** (Fig. 1a). For **SiO_2-PYZ** nanocomposites, after pore expansion of synthesized materials, the Si-OH vibration band decreased by about 560 cm^{-1} due to the interaction between $–NH_2$ groups and groups of silanol *via* the hydrogen bonding. The peak of 1087 cm^{-1} comes from the Si-O vibration in the bulk silica. At 1637 cm^{-1} and 3400 cm^{-1}, peaks are usually ascribed to the silica-pulp surface adsorbed water.

Observing N-H bending vibrations at 692 cm^{-1} verifies the incorporation of the $–NH_2$ group into mesoporous **MCM-41**. For **MCM-41**, the vibration modes were located as follows; 3423 cm^{-1}(–OH), 1089 cm^{-1}, 796 cm^{-1} (Si–O–Si), 970 cm^{-1} (Si-OH), and 471 cm^{-1} (Si–O). When compared to the strength of the Si-OH vibration at 970 cm^{-1} in unmodified mesoporous **MCM-41**, the intensity of the -Si-OH vibration at 970 cm^{-1} in $–NH_2$ mesoporous **MCM-41** reduced, indicating that the modification had occupied most of the -Si-OH bonds on the inner surface of **MCM-41**.

The absorption of C-N stretching vibrations is usually about 1200–1000 cm^{-1}, but this band, due to its overlap with Si-O-Si absorption, can stretch in the range 1000–1238 cm^{-1}, Si-CH_2-R, which lengthens to 1153–1250 cm^{-1} are not permitted. The band at 876.34 cm^{-1} in the FTIR spectra of **SiO_2-PYZ** nanocomposites demonstrates S-H bending. Furthermore, at frequencies 3440, 3259, 1658, 1471, and 767 cm^{-1}, distinct absorption bands were ascribed to OH, NH, C = O, N = N, and C–Cl. **SiO_2-PYZ** nanocomposite shows C-O stretching at 699 cm^{-1} in mesoporous **MCM-41**.

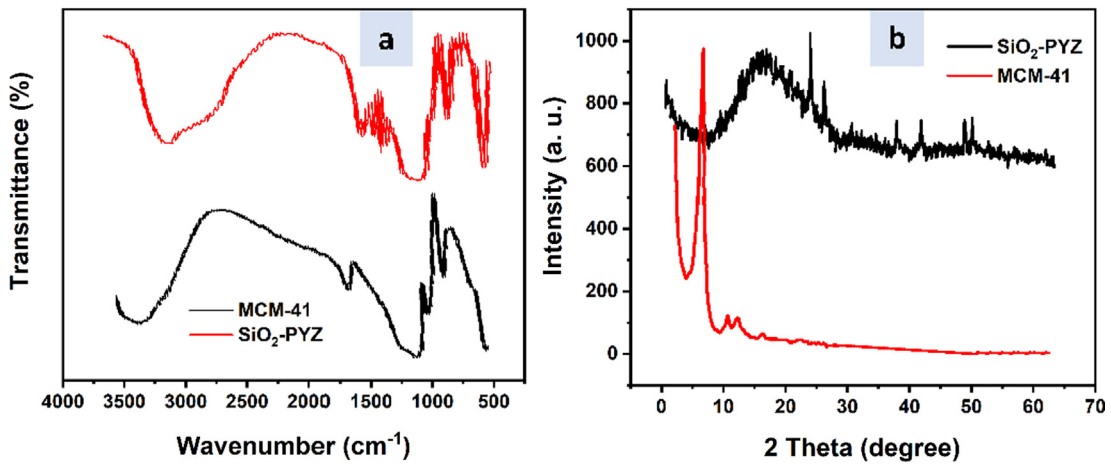

Fig. 1 (a) FTIR and (b) XRD analysis curves of nanoparticles; mesoporous silica **MCM-41** and **SiO_2-PYZ** nanocomposite.

3.2.2. XRD

XRD has investigated the amorphous and crystalline nature of mesoporous silica and nanocomposites **SiO_2-PYZ** with an appropriate formulation. The XRD pattern demonstrates that the mesoporous silica nanoparticle is crystalline, as seen in Fig. 1b. A mesoporous silica nanoparticle exhibits two peaks in XRD examination, at 6.5° and 23°, imprintingthat the mesoporous **MCM-41** silica particles are of crystallinity nature (El-Maghrabi, 2017; Slowing et al., 2006).

With the above-described peaks, **SiO_2-PYZ** nanocomposites show a broad peak between 20° and 30° in mesoporous silica **MCM-41**. This amorphous peak can signify the nanoparticles' peak in silica. The inclusion of a silica coating also reduces XRD peak intensity.

Besides a broad peak ascribed to the **SiO_2**, there are two diffraction peaks at $2\theta = 16°$, indicating the presence of **PYZ** in the structures of **SiO_2-PYZ** nanocomposites that decrease its crystallinity concerning mesoporous silica. However, only a very sharp peak of **SiO_2-PYZ** at 24°, 26.1°, 37.9°, 41.8°, and 48.8°, respectively. These peaks indicated small particles with the semi-crystalline nature of nanocomposite.

3.2.3. SEM

As shown in Fig. 2a, the mesoporous silica nanoparticles' diameter is between 0.2 and 0.5 μm, indicating the high surface area and porosity. The size is almost unchanged for the **SiO_2-PYZ** nanocomposite core–shell (Fig. 2b). Still, the topography has changed where the surface becomes rough, and the porosity has increased due to the coordination of chemical interaction between the two materials. The core–shell structure formation was the silica nanoparticles in the core covered with a connected hairy layer of the prepared **SiO_2-PYZ** that acts as a semi-permeable membrane. The existence of this thin layer increases adsorption and selectivity towards metal ions.

3.2.4. TGA

Fig. 3 presents the TGA curves of mesoporous silica **MCM-41** and **SiO_2-PYZ** nanocomposites. Initial losses at temperatures below 100 °C in nanocomposite samples of mesoporous silica and **SiO_2-PYZ** because of the physically absorbed water and some residues from hydrolysis reactions due to surfactant presence. The weight loss after 200 and 800 °C was due to the loss of organic working groups in the mesoporous walls. The condensing of Si-OH units on the pore walls can also create water

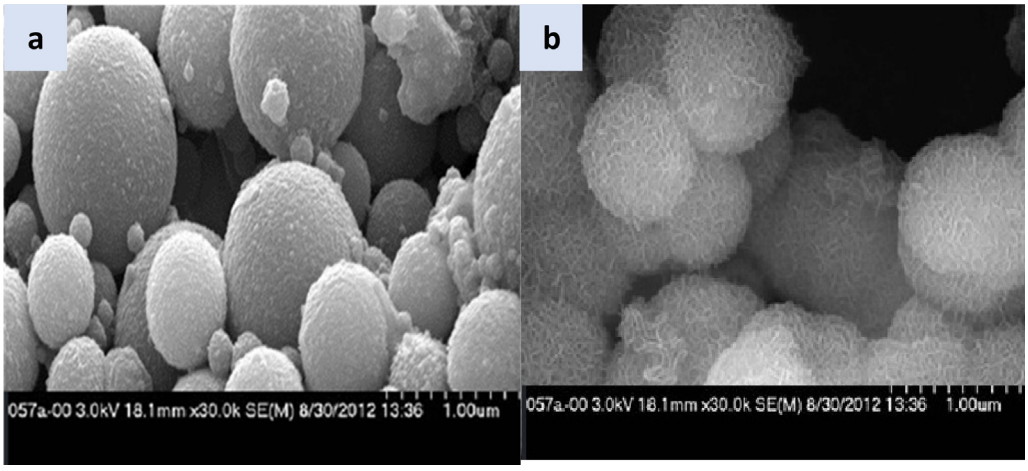

Fig. 2 SEM texture of (a) mesoporous silica **MCM-41** and (b) **SiO_2-PYZ** nanocomposites.

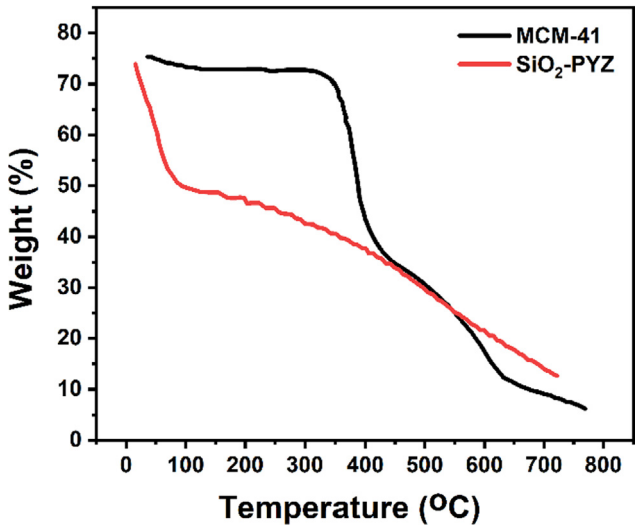

Fig. 3 TGA curves of mesoporous silica **MCM-41** and **SiO_2-PYZ** nanocomposites.

molecules during this process. Between 100 and 400 °C, the total weight loss of **SiO_2-PYZ** nanocomposites was ~ 41.2%, much higher than that of mesoporous silica (~10%). This difference in weight loss could be accounted for by the amount of conjugated **PYZ** (about ~ 12.1%). The functionalized sample also offered better stability than pure **PYZ**, which is shown to have a complete degradation at around 600 °C. Together with FT-IR, the data from TGA confirmed the coating of **PYZ** onto the mesoporous silica (**MCM-41**) surface.

3.2.5. TEM

The **MCM-41** and **SiO_2-PYZ** preparation morphology was characterized by TEM. In the case of **MCM-41** (Fig. 4a-c) with different magnifications, the silica was arranged in a harmonious state with an ordered structure. The shape was uniform mesopores honeycomb with a hexagonal array. The low magnification TEM photo shows a clear center (cavity) and a dark **SiO_2-PYZ** nanocomposite with an open structure, as shown in Fig. 4d. Besides, there was a relatively consistent diameter below 20 nm in the hollow spheres. The hollow sphere consisted of interconnected nanocrystals varying between 2 and 3 nm in size, shown in the substantially higher magnification TEM image.

3.3. Batch adsorption process for SiO_2-PYZ nanocomposite

3.3.1. Kinetics

The influence of retention time on the uptake of Zn(II) and Cr (III) (Qe, mg/g) with varying adsorbent concentrations are shown in Fig. 5a,b. There are three different waves of adsorption behavior. As adsorption time is frequently from 5 to 110 min, first no change is observed in the adsorption, further increased to 275.5 mg/g at 500 mg/l for Zn(II) uptake was attained. A similar trend was obtained in Cr(III), although with higher adsorption with higher uptake of 380 mg/g at 500 mg/l and afterward a slow kinetic rate within which 422.9 mg/g Cr(III) adsorption. Overtime, adsorbent surface coverage becomes high and poor absorption occurs. The evolution of Zn(II) and Cr(III) uptake over time is shown in Fig. 5.

The initial rapid increase in adsorption can be associated with free adsorption sites on **SiO_2-PYZ** and unrestricted active

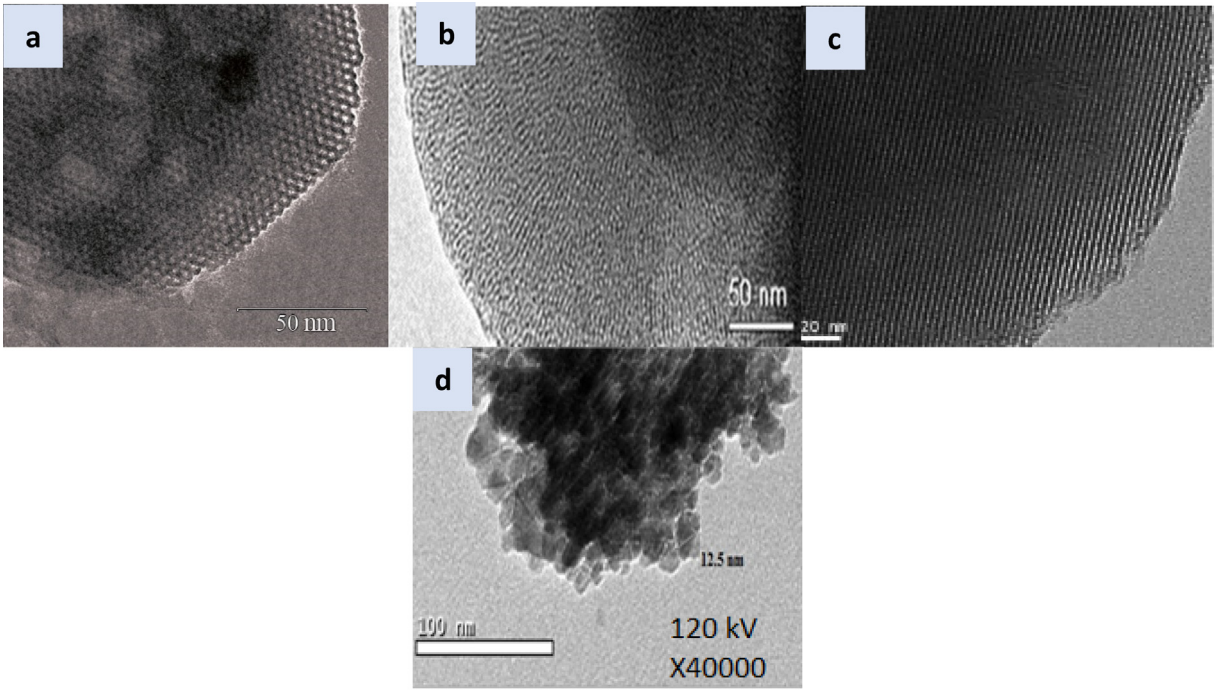

Fig. 4 TEM analysis of (a-c) **MCM-41** at different views, (d) **SiO_2-PYZ** nanocomposites.

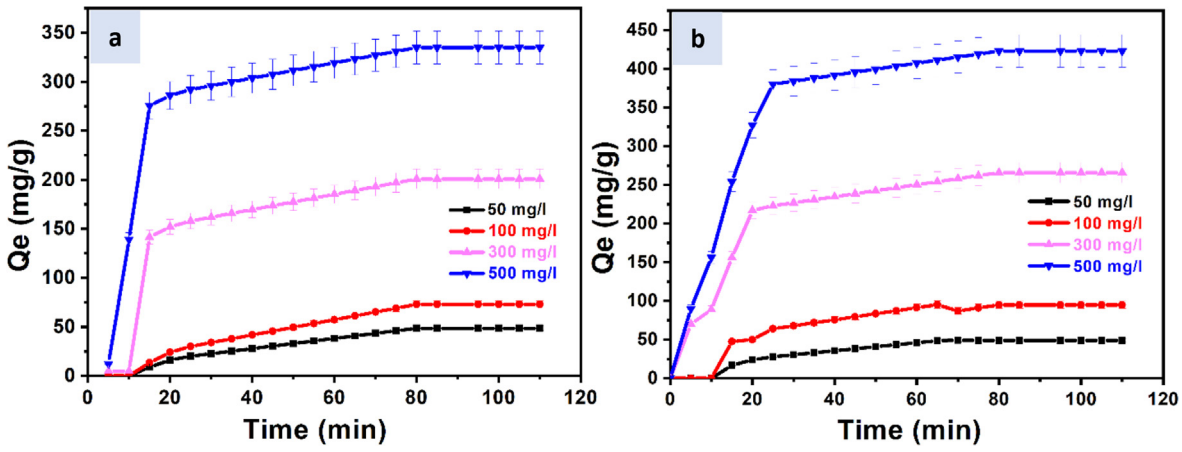

Fig. 5 Effect of retention time on the adsorption of (a) Zn(II) and (b) Cr(III) on **SiO_2-PYZ** nanocomposite [pH = 7, T = 25.5 ± 2 °C, dosage = 1 gm].

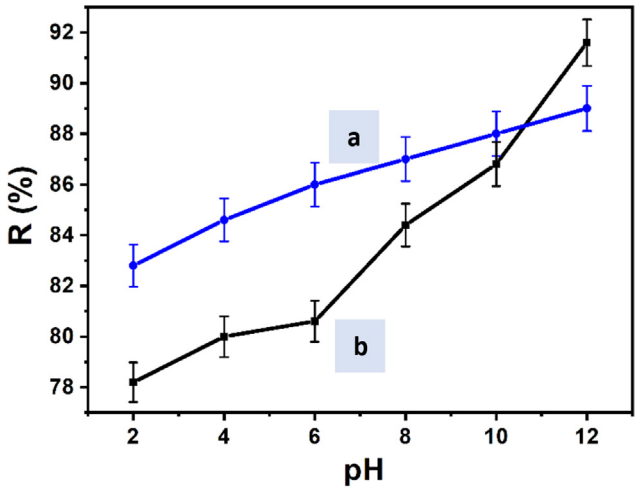

Fig. 6 Influence of pH on the adsorption of (a) Zn(II) and (b) Cr (III) on **SiO_2-PYZ** nanocomposite [time = 120 mins., T = 25.5 ± 2 °C, adsorbent weight = 1 gm and Co = 500 mg/l].

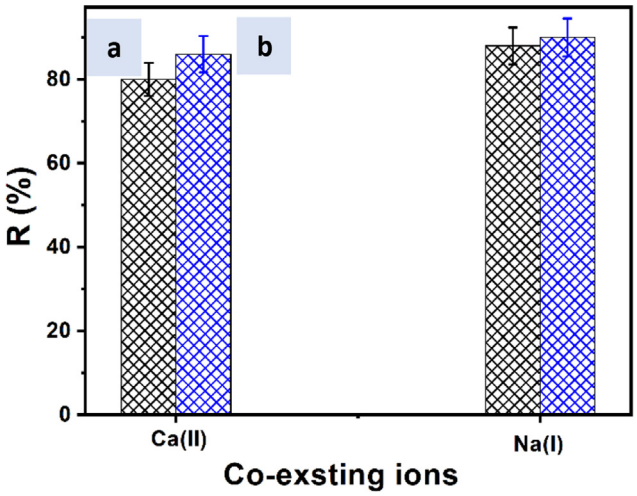

Fig. 7 Effects of coexisting ions (Ca(II) and Na(I)) on the removal of (a) Zn(II) and (b) Cr(III) ions from water solution by **SiO_2-PYZ** nanocomposite [time = 120 min, pH = 7, T = 25.5 ± 2 °C, adsorbent weight = 1 gm and C_o = 500 mg/l].

sites with similar energies. Nevertheless, the adsorption rate slows as more and more active sites are filled, and adsorption becomes harder until the balance has been achieved. In a simple and binary solution, the quantity of Cr(III) adsorbed at all times was more remarkable than the quantity of Zn(II) in the solution.

3.3.2. Effect of pH

Fig. 6 illustrates pH variation on the **SiO_2-PYZ** nanocomposite adsorption with similar duration and concentration of adsorbate. The solution's pH was between 1 and 13, and it was obtained that Zn(II) and Cr(III) ion removal efficiency was 91.9 and 89 %, at pH 12. With increasing pH, adsorbed quantities have risen so that Zn(II) is more affected than Cr (III). Zn(II) and Cr(III) ions' adsorption can often be pH-dependent. The adsorbent controlled the pH from + 3 to + 6, with reducing centers that prevent the conversion action as it has -NH and -OH groups that act as reducing. In each case, the partially negative reacts with the somewhat positive metal of the substrate.

3.3.3. The co-existing ions effect

The co-existing cations effects were studied, and the data are shown in Fig. 7. Adsorption by **SiO_2-PYZ** nanocomposite was studied with Ca(II) and Na(I) interfering ions. These ions showed a minor effect on Zn(II) and Cr(III) adsorption. A negligible impact of co-existing cations on Cr(III) removal by **SiO_2-PYZ** was found due to the stronger bonds of Cr (III) to surface sites of **SiO_2-PYZ** when Ca(II), Na(I), and other cations co-existed in the water solution. These ions may participate in active adsorption sites on the surface of **SiO_2-PYZ** with Zn(II) ions, as the Zn(II) removal was reduced by ~ 20–25% and ~ 30–32%, respectively, when Ca(II) and Na(I) were present. Compared to Zn(II), the composite had

superior selectivity and adsorption affinity for Cr(III). The results indicated that in the water solution, the given **SiO_2-PYZ** nanocomposite had high adsorption capability towards Cr(III) ion compared to Zn(II) ion.

3.3.4. Effect of different metal ion concentrations

The effect of initial ion concentrations of Zn(II) and Cr(III) on adsorption efficiency for **SiO_2-PYZ** nanocomposite was studied by experimenting with several ions 'initial concentrations of 50–500 mg/l at the constant retention time, adsorbent dosage, and temperature. The pH of solutions was controlled (pH 12), and the adsorption process was conducted for one hour at a speed of 500 rpm.

The adsorption efficiency was changed from 99.8% to 85.9% at the original concentration. Although Zn(II) and Cr (III) adsorption effectiveness reduces with an increment of the starting concentration, the change is only highly minor. The initial concentration shows that the adsorption processes are only minimally affected (Fig. 8).

3.3.5. Effect of dosages

The effect of the prepared **SiO_2-PYZ** nanocomposite adsorbent doses is shown in Fig. 9. As the adsorbent dosage increases, the adsorption efficiency of Zn(II) and Cr(III) ions increases. The maximum adsorbent dosage of the prepared **SiO_2-PYZ** nanocomposite is 1 gm with a removal efficiency of ~ 87.8 and 93% for Zn(II) and Cr(III) ions, respectively. At which lower adsorbent dosage, the number of active sites is lower than the available ions concentration in the bulk solution.

3.3.6. Effect of adjusted temperature

Fig. 10 studies the influence of temperature over a specific value starting from 25 °C up to 66 °C with pH 12. The removal percentage of Zn(II) onto **SiO_2-PYZ** nanocompositewas increased with an increase in temperature up to 60 °C, 87.2 % removal, and then decreased when the temperature

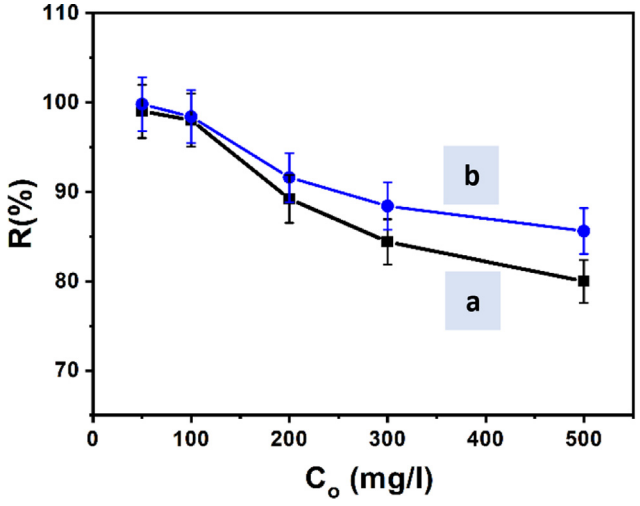

Fig. 8 The effect of initial metal ions concentrations on the efficiency of the adsorption processon (a) Zn(II) and (b) Cr(III) [time = 120 mins., pH = 7, T = 25.5 ± 2 °C, adsorbent weight = 1 gm].

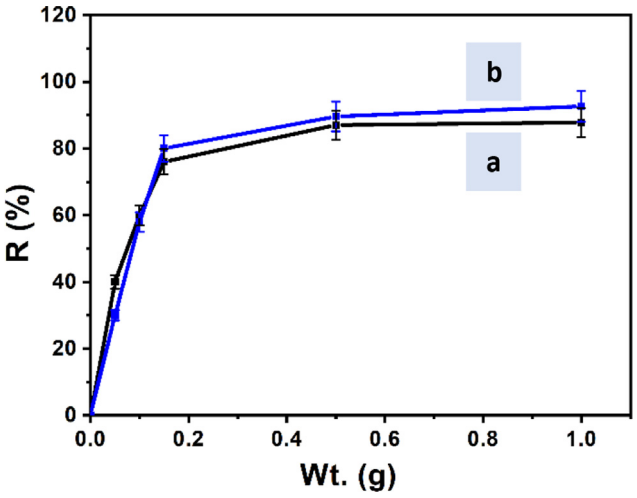

Fig. 9 Effect of adsorbent dosage of **SiO_2-PYZ** nanocomposite on the removal efficiency of (a) Zn(II) and Cr(III) [time = 120 mins., pH = 7, T = 25.5 ± 2 °C, adsorbent weight = 1 gm].

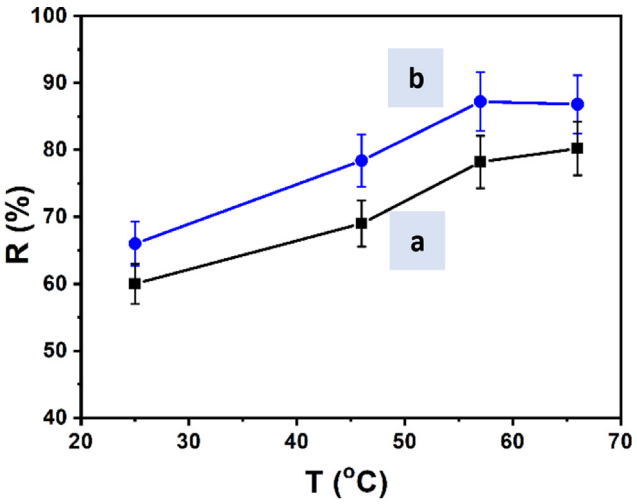

Fig. 10 Effect of temperature on the adsorption of (a) Zn(II) and (b) Cr(III) on **SiO_2-PYZ** nanocomposite [time = 20 mins., pH = 7, adsorbent weight = 1 gm, and Co = 500 mg/l].

was further raised. The removal percentage of Cr(III) onto **SiO_2-PYZ** nanocomposite was increased with increased temperature up to 66 °C, reaching 80.2%. Intraparticle diffusion increases at high temperatures, and more adsorption sites are created, which boost adsorption.

3.4. Linear and nonlinear kinetic models

3.4.1. Pseudo-first-order (PFO) kinetic model

According to the PFO model, the rate of change in Zn(II) and Cr(III) adsorption capacity with time is proportional to the difference between the equilibrium concentration and the amount of Zn(II) and Cr(III) adsorbed over a time range. This type was insufficient to illustrate the kinetic behavior of selected metal ions on **SiO_2-PYZ** nanocomposite, at least in

Table 1 Adsorption kinetics and dynamic molding of Zn(II) and Cr(III) ions on **SiO_2-PYZ** nanocomposite.

Adsorption Models	**Adsorption Parameters**			
PFO	$C_0(mg/l)$	K_1	Q_e	R^2
	Zn (II)			
	50	0.0170	0.2998	0.9351
	100	0.0071	0.3167	0.9948
	300	0.0052	0.3802	0.8798
	500	0.0046	0.4076	0.8159
	Cr (III)			
	50	0.0109	0.3233	0.9640
	100	0.0146	0.3074	0.9288
	300	0.0084	0.3492	0.9115
	500	0.0109	0.4098	0.9079
PSO	C_0	q_e	k_2	R^2
	Zn (II)			
	50	345.60	0.0029	0.9627
	100	359.63	0.0028	0.9803
	300	100	0.01	1
	500	500	0.002	1
	Cr (III)			
	50	134.54	0.0074	0.9852
	100	530.61	0.0019	0.9281
	300	101.79	0.0099	0.9992
	500	505.92	0.0020	0.996
Intra particles	$C_0(mg/l)$	A	k_d	R^2
	Zn (II)			
	50	0.0776	17.701	0.7484
	100	0.0776	19.374	0.7484
	300	0.0928	25.209	0.7078
	500	0.0673	17.701	0.6394
	Cr (III)			
	50	0.0633	13.774	0.6803
	100	0.0633	15.071	0.6803
	300	0.0538	13.384	0.6465
	500	0.0556	13.774	0.6451

its linear form. Despite the use of suitable linear regression coefficients (R^2), no linear trend was observed when the experimental data was plotted for the entire Zn(II) and Cr(III) nominal concentrations. Both Zn(II) and Cr(III) reactions on **SiO_2-PYZ** nanocomposite were poor linearities, regardless of higher linear regression coefficients.

In the current study, unknown logarithmic values hindered the PSO linear model from fitting better. Thus, for both pHs tested, the PFO adsorption rate constants (k_1) were negative and of a small order of magnitude, maybe suggesting deprived affinity or repulsion between Zn(II) and Cr(III) solutions and **SiO_2-PYZ** nanocomposite. Recently, machine learning (ML) has gained fame in material science, and it is an easy and fast method. When it comes to computing, ML is a branch of computer science that uses algorithms and techniques to automate solutions to complex problems that are difficult to program using conventional programming methods (Mahmood and Wang, 2021; Mahmood and Wang, 2021; Mahmood and AhmadIrfan, and Jin-LiangWang, , 2021; Mahmood et al., 2022).

For the dynamic conditions of Zn(II) and Cr(III) adsorption, PFO kinetic model was considered as follows:

$$\text{PFO equation} : \log(Q_e - Q_t) = \log Q_e - K_1 t \tag{3}$$

3.4.2. Pseudo-second-order (PSO) kinetic model

The PSO kinetic model was used to describe the efficiency of the adsorption process. Zn(II) and Cr(III) adsorption onto **SiO_2-PYZ** nanocomposite obeyed PSO kinetics in linear and non-linear forms. Moreover, PSO constant rates (k_2) were similar when comparing the linear and nonlinear models at the same pH, but upper initial adsorption rates (h) were recorded for the nonlinear model. Higher linear $R^2 \approx 1.0$ and sharp comparison between experimental and calculated adsorption at equilibrium ($\sum\chi^2 < 0.05$) suggested a better fit with the linear than the nonlinear model ($\sum\chi^2 < 0.50$), but being nonetheless, the two values were comparatively lower than the Chi-square tabular value (9.488). A very small Chi-square test indicates that the calculated data is well-matched with the experimental data. As a result, the PSO kinetic model fit was greatly improved rather than PFO.

$$\text{PSO equation} : \frac{t}{q} = \frac{1}{K_2 q_e^2} + \frac{t}{q_e} \tag{4}$$

3.4.3. Intra particles kinetic model

The intra particles equation is expressed by the following:

$$\text{Intra particles equation} : q = K_d t^{1/2} + a \tag{5}$$

Table 2 MSE-percentage error and Chai-square of adsorption kinetics and dynamic molding for **SiO_2-PYZ** nanocomposite towards Zn(II) and Cr(III).

Adsorption model	C_o (mg/l)	MSE-Percentage error	Chai-square X^2
	Zn(II)		
PFO	50	30,692	72.772
	100	30,692	70.140
	300	30,692	67.507
	500	30,692	64.875
	Cr(III)		
	50	128,764	37.979
	100	128,764	41.379
	300	128,764	44.779
	500	128,764	48.170
PSO			
	Zn(II)		
	50	61,385	84.807
	100	60,681	92.400
	300	49,678	99.992
	500	26,882	107.58
	Cr(III)		
	50	29,616	26.231
	100	29,381	28.580
	300	26,882	30.928
	500	26,882	33.277
Intra particles	Zn(II)		
	50	148,378	186.57
	100	148,478	203.28
	300	134,458	219.98
	500	134,959	236.68
	Cr(III)		
	50	3238.6	83.554
	100	3214.9	91.034
	300	2955.5	98.514
	500	2965.2	105.99

where q, a, and k_d represent the optimal amount of solute adsorbed (mol /g), intercept, and the intraparticle diffusion rate constant (mol/g $min^{1/2}$).

Plotted t/q against t of the PSO reaction for the adsorption of Zn(II) and Cr(III) on **SiO_2-PYZ** nanocomposite was used to detect the rate parameters. These plots derived the kinetic parameters under various conditions listed in Table 1. The results show that Zn(II) and Cr(III) adsorption on **SiO_2-PYZ** nanocomposite does not follow PFO or intraparticle kinetics.

The slope of the linear plot of t/q_t vs. t was $1/q_e$, and the intercept was $1/k_2q_e^2$. This method is more likely to anticipate behavior across the entire adsorption range. A linear plot of t vs. t/q_t matches the experimental and estimated q_e values (Table1). Furthermore, the correlation coefficient values for the PSO model were nearly equal to unity for all Zn(II) and Cr(III) ions concentrations, indicating that the PSO model can be used to define the adsorption process of Zn(II) and Cr(III) ions on the prepared **SiO_2-PYZ** nanocomposite. In this case, the adsorption property follows a physisorption mechanism. The rate of approach to equilibrium is often increased as temperature rises, but the equilibrium adsorption capacity decreases (Rahman and Varshney, 2021).

Furthermore, to select a better model that fits the experimental data, Chi-square (χ^2), the mean square error (MSE), and correlation coefficient (R^2) listed in Table 2 were used to justify the favored adsorption kinetic model. Table 2 shows the MSE-percentage error and Chai-square of adsorption kinetics and dynamic molding of Zn(II) and Cr(III) ions on **SiO_2-PYZ** nanocomposite. The smaller the χ^2 value, the closer the agreement in the fit between the experimental data and linearized forms of the kinetic equations.

3.5. Adsorption isotherm

The Freundlich model depicts multilayer adsorption, while the Langmuir isotherm represents monolayer adsorption. The Langmuir isotherm is given by Eq(6):

$$q = \frac{q_0 K_L C_t}{1 + K_L C_t} \tag{6}$$

Assume that q is the maximum quantity of metal ion mg/g of adsorbent from a complete monolayer on the surface, C_t is the equilibrium concentration, K_L is a constant related to binding site affinity, and q_0 is the maximum amount of metal ion (mg) per unit weight (g) of adsorbent. As seen below, the Langmuir equation can be represented in a variety of ways:

$$\frac{C_t}{q} = \frac{C_t}{q_0} + \frac{1}{K_L q_0} \tag{7}$$

The equation gives Freundlich isotherm.

$$q = K_f C_t^{1/n} \tag{8}$$

K_F (mg/g) and n are the Freundlich adsorption isotherm constants, indicating the adsorption extent and the nonlinearity degree between adsorption and solution concentration. Taking logarithm on both sides.

$$\log q = \log k_f + \frac{1}{n} \log c_t \tag{9}$$

The Freundlich constant n measures the deviation from linearity of the adsorption and is used to verify the adsorption type. If n is equal to unity, the adsorption is linear. If n below unity indicates that adsorption is a chemical process, n above unity is associated with favorable adsorption and a physical process (Rahman et al., 2020; Rahman et al., 2020). The adsorption of Zn(II) and Cr(III) ions by **SiO_2-PYZ** nanocomposite fit both the Langmuir and Freundlich adsorption isotherm equations with R^2values greater than 0.9. The Langmuir isotherm presupposes a homogenous monolayer of adsorbate covers the adsorbent (Rahman and Varshney, 2020; Rahman and Haseen, 2014). The Freundlich isotherm equation presupposes that multiple surface layers surround the adsorbent (multilayer) and are heterogeneous. In this study, the highest adsorption capacity of Zn(II) and Cr(III) ions by **SiO_2-PYZ** nanocomposite particles was 0.094 mg/g for Zn(II) and 0.642 mg/g for Cr(III) ions, respectively. Tables 3 and 4 clarify the mathematical calculation of linear and nonlinear Langmuir and Freundlich adsorption isotherms of Zn (II) and Cr(III) ions by **SiO_2-PYZ** nanocomposite at different temperatures.

Nonlinear regression is the most practical method for determining the isotherm model parameters. The obtained data from nonlinear regression are more suitable than those obtained from linear one. Different forms of nonlinear regres-

Table 3 The linear Langmuir and Freundlich adsorption isotherms of Zn(II) and Cr(III) ions by **SiO_2-PYZ** nanocomposite at different temperatures.

Isotherm equation	Temperature (K)			
	298	319	330	339
	Zn(II)			
Langmuir				
q_o (mg g $^{-1}$)	0.0930	0.0945	0.0715	0.0876
K_L (L mg^{-1})	0.0039	0.0038	0.0036	0.0039
R^2	0.9429	0.9143	1	0.9452
Freundlich				
K_f	0.6420	0.5006	0.5401	0.5332
n	0.4436	1.3653	1.2823	1.3587
R^2	0.9990	0.9649	0.9912	0.9891
	Cr(III)			
Langmuir				
q_o (mg g $^{-1}$)	0.0419	0.0731	0.0582	0.0367
K_L (L mg^{-1})	0.0041	0.0034	0.0031	0.0042
R^2	0.9378	0.9003	0.9451	0.9399
Freundlich				
K_f	0.4778	0.3643	0.3370	0.3530
n	0.1016	1.6703	1.7253	1.7262
R^2	0.9859	0.9808	0.9816	0.9857

Table 4 The non-linear Langmuir and Freundlich adsorption isotherms of Zn(II) and Cr(III) ions by **SiO_2-PYZ** nanocomposite at different temperatures.

Zn(II)		
Ce	Langmuir isotherm	Freundlich isotherm
5	26.3488	26.3488
10	27.3493	31.5071
54	36.1541	49.371
78	40.9566	54.419
Cr(III)		
Ce	Langmuir isotherm	Freundlich isotherm
1	25.548	49
8	26.949	92
42	33.753	158
58	36.954	242

sion can be applied. Various isotherm models (Table 5) were considered for the nonlinear regression analysis to define the adsorption process. To compare the results of the linear and nonlinear regression analyses, the standard deviation (S_D) and coefficients of determination (R^2) were calculated for each of the variables.

Fig. 11a-f show linear and non-linear Langmuir and Freundlich for Zn(II) and Cr(III). Even linear or nonlinear matching with the experimental range, especially with the Freundlich system, yields a high R^2. Linear and non-linear fitting yielded vastly different results in the error analysis. Findings suggest a significant improvement in prediction accuracy by using a non-linear fit to the Freundlich isotherm instead of a linear fit. According to the data, it presents favorable adsorption, the values for the constant n were around 1 when using **SiO_2-PYZ** nanocomposite as an adsorbent for both linear and non-linear fitting. Using non linearized regression, the results showed much higher q_m values. In other words, the nonlinear fitting of measured data to a non-linearized form of the Freundlich model depicted a greater affinity between experimental and predicted data than the linearization of a Freundlich isotherm. It was found that using the non-linear Freundlich isotherm yielded more reliable results with higher R^2 and smaller error sum of squares.

3.6. Comparison with other sorbents

Table 6 displays the related studies on heavy metal Zn(II) and Cr(III) adsorption of various prepared adsorbent materials, summarizing the relevant adsorption capacity. To prove the effectiveness of **SiO_2-PYZ** nanocomposite as a strong adsorbent, its adsorption capability must be compared to that of other adsorbents. The data shows the capacity values mentioned in the literature. Compared to other adsorbents, it demonstrates that **SiO_2-PYZ** nanocomposite has a high

Table 5 Equilibrium model equations investigated Zn(II) and Cr(III) adsorption onto **SiO_2-PYZ** nanocomposite.

Isotherm	Nonlinear equation	Linear equation
Langmuir	$q_e = q_{max} \cdot K_L \cdot C_{e1} + K_L \cdot C_e$	$1q_e = 1q_{max} + 1q_{max} \cdot K_L \cdot 1C_e$
Freundlich	$q_e = K_F \cdot C_e 1/n$	$\log q_e = \log K_F + 1n \cdot \log C_e$

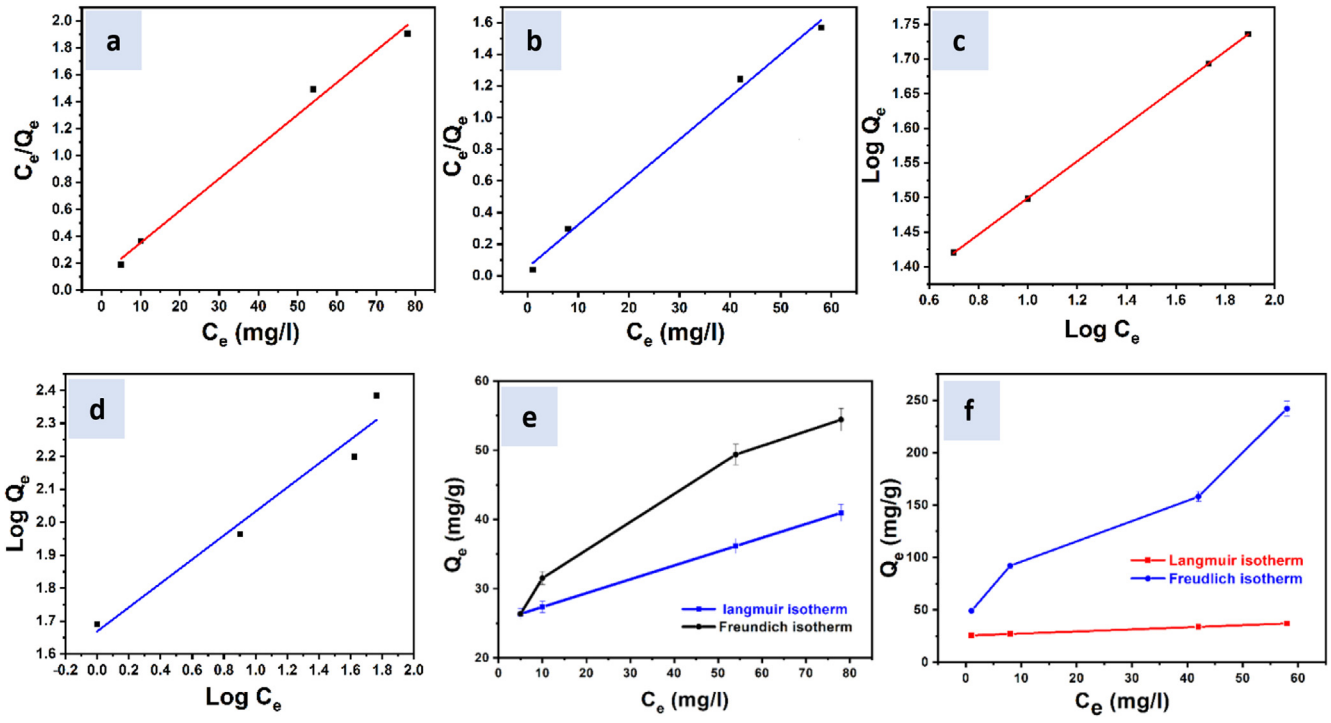

Fig. 11 Non-Linear Langmuir isotherm of (a) Zn(II) and (b) Cr(III), Non-Linear Freundlich isotherm of (c) Zn(II) and (d) Cr(III), and Linear fit of Langmuir isotherm of (e) Zn (II) and (f) Cr(III) adsorption by **SiO_2-PYZ** nanocomposite.

Table 6 General comparison between the different adsorbent systems in literature and **SiO_2-PYZ** nanocomposite.

Adsorbent	Pollutant	Conc. (mg/l)	Capacities (mg/g)	Ref.
Thiol-functionalized mesoporous calcium silicate (MCS-SH)	Cd(II), Cu(II), Pb(II), and Cr(III)	25, 50, 75, 100, 125, and 150	601.51, 509.56, 618.09, and 334.81	(Lihua, 2017)
Silicagel modified with salicylaldoxime	Zn(II)	1–10	2.61	(Üçer et al., 2006)
$NiFe_2O_4$/ZnAl-EDTA LDH	Cr(VI)	50	77.22	(Deng, 2017)
Steel slag	Cr(III), Zn(II)	500	105.26, 42.19	(Chen, 2019)
Fungus Phallus impudicus loaded γ-Fe_2O_3 nanoparticles	Cr(III), Zn(II)	50–150	22.8, 25.6	(Yalçın, 2020)
MCS-SH	Cr(III)	150	334.81	(Silva, 2020)
Fe_3O_4@SiO_2 magnetic	Zn(II)	20	170	(Wamba, 2018; Hao, 2016)
Amino-functionalized mesoporous silicas (AFMS)	Zn(II)	0.1 to 4 mM	89	(Toor et al., 2019)
Synthesized Silica @Based @ MCM-41	Zn(II), Cr(VI)	50	392, 554	(Rahman and Varshney, 2021)
SiO_2-PYZ nanocomposite	Zn(II), Cr(III)	1000	850, 500	**This Study**

adsorption capacity. Different adsorbent features, such as structural characteristics, functional moieties, and surface areas, are attributed to variances in metal ion adsorption ability (Ozsoy and Kumbur, 2006).

3.7. *Thermodynamics*

The thermodynamics study on adsorption is exciting and enables us to know if the specific adsorption process is chemical or physical, spontaneous or non-spontaneous exothermic or endothermic. First, the influence of temperature (T) on the adsorption process is examined (Fig. 12).

The following parameters, Gibb's free energy ΔG, enthalpy ΔH, and entropy ΔS, are thermodynamic factors that are suggestive of the likely type of adsorption and represented by the Van't-Hoff equations Eqn 10, 11 and 12:

$$\Delta G = \Delta H - T\Delta S \tag{10}$$

$$\Delta G = -RT \ln K_d \tag{11}$$

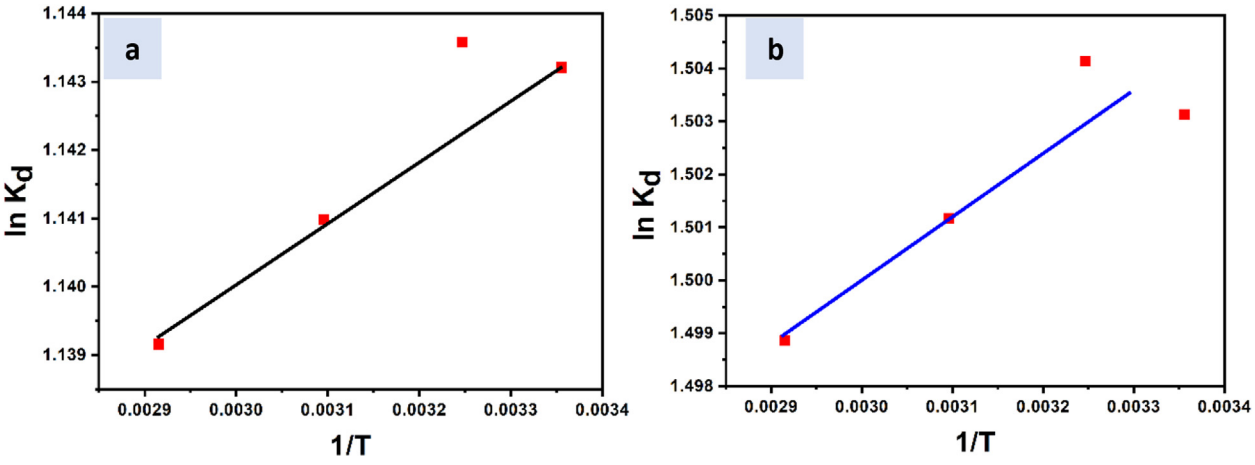

Fig. 12 Dependency of *ln* K_d on 1/T used for the adsorption of (a) Zn(II) and (b) Cr(III) on **SiO_2-PYZ** nanocomposite.

Table 7 Thermodynamic parameters of Zn(II) and Cr(III) ions removal from aqueous solution by **SiO_2-PYZ** nanocomposite.

Metal ion	Temp. K	ΔS (J/mol. K)	ΔH (KJ/mol)	ΔG
Zn(II)	298	330.57	−3064.5	−2831.7
	319	0	0	−2927.7
	330	0	0	−3063.3
	339	0	0	−3247.8
Cr(III)	298	437.06	−3323.6	−3723.2
	319	0	0	−3850.7
	330	0	0	−4030.3
	339	0	0	−4273.3

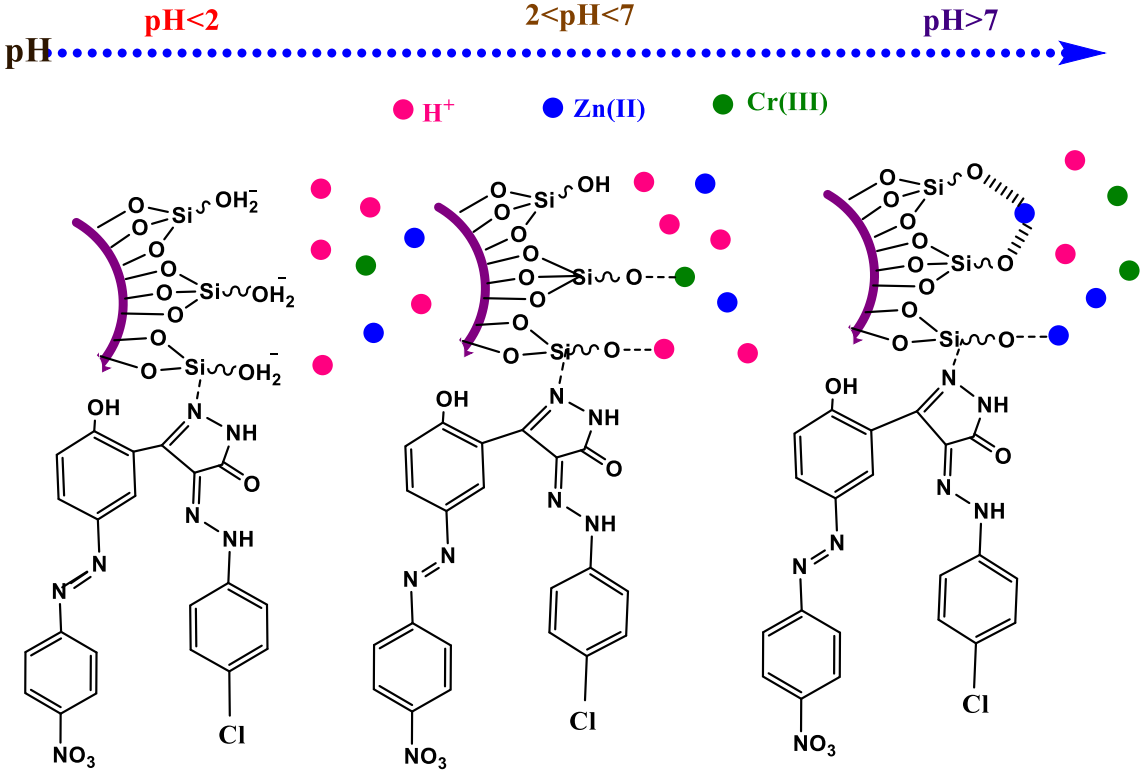

Fig. 13 Adsorption mechanisms of **SiO_2-PYZ** nanocomposite under different pH values.

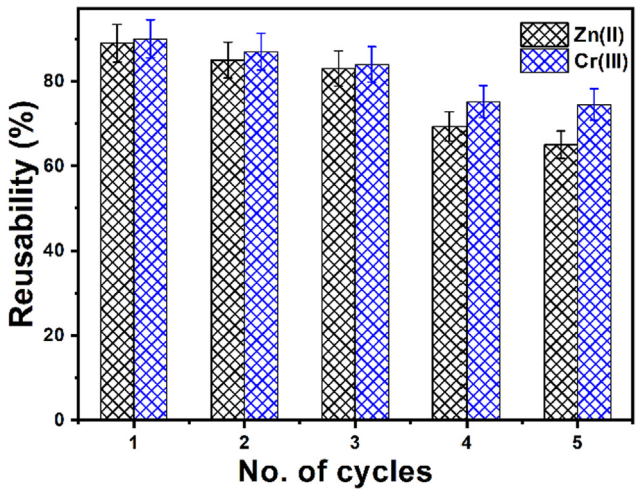

Fig. 14 The reusability performance of **SiO_2-PYZ** nanocomposite adsorbent [time = 120 mins., pH = 7, T = 25.5 ± 2 °C, adsorbent weight = 1 gm, and Co = 500 mg/l].

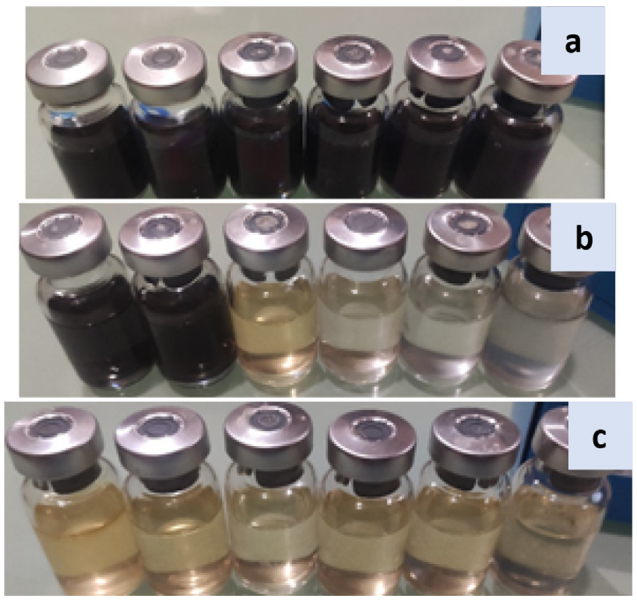

Fig. 15 Infected water samples with varying **SiO_2 -PYZ** concentrations were introduced into SRB growth measurement media kits (a) blank, (b) 20 mg/l, and (c) 40 mg/l.

R is the gas constant, T is the temperature (K), and K_d is the thermodynamic equilibrium constant of the Zn(II) and Cr(III) adsorption on the prepared **SiO_2-PYZ** nanocomposite. During plotting of $\ln K_d$ vs. 1/T, ΔH and ΔS were estimated from Van't-Hoff equation's slope and intercept (Fig. 12) (Bennet, 2017).

$$\ln k_d = \frac{\Delta S}{R} - \frac{\Delta H}{RT} \tag{12}$$

The influence of temperature on the adsorption behavior is to be first analyzed. The values of Gibbs free energy (ΔG) for various temperatures are recognized from the experimental data. The slope and intercept of the curve between $\ln K_d$ and 1/T can determine the enthalpy change values (ΔH) and entropy change (ΔS). We can evaluate thermodynamic feasibility, spontaneity, and thermal effects of sorption from these thermodynamic parameters. Table7 summarizes the results for thermodynamic parameters.

The results reveal that the value ΔG of Zn(II) and Cr(III) is negative at all temperature ranges and increases with temperature, indicating that adsorption on the adsorbents is spontaneous as the feasibility of the adsorption reaction increases. At low temperatures, sorption efficiency improved with a decrease in ΔG. As the negative value of ΔG raised with temperature, the adsorption behavior becomes more favorable at lower temperatures, demonstrating the conventional physical adsorption mechanism.

3.8. Adsorption mechanism

The impact of pH on the adsorption process can be explained based on the nature of the isoelectric point of silica material at pH = 2, which is determined by its zeta potential. Silica surface is positively charged below = 2, so the interaction between the adsorbent and the metal ions is electrostatic repulsion; hence, the higher the repulsion, the lower the pH value. Also, at common pH values, sometimes precipitation and formation of hydroxides are dominant, hindering the adsorption process. Increasing pH more than 2, the surface of silica becomes more negative; consequently, the whole inner channels and the surface of **SiO_2-PYZ** nanocomposite become more energetic with a negative charge. These criteria enhance the electrostatic attraction between adsorbent and adsorbate, and more removal capacity will attain. The presence of H^+ ions in the solution with Zn(II) and Cr(III) significantly attracted more negative charged groups inside the channels and surface of **SiO_2-PYZ** nanocomposite when the pH is acidic, and the same positive charges interfere, causing competitive adsorption between H^+ and metal ions Zn(II) and Cr(III). Otherwise, the active adsorption sites on the **SiO_2-PYZ** nanocomposite surface are filled by H^+, reducing the adsorption of Zn(II) and Cr(III). Increasing controlled pH value, silanol groups in harmony with H^+ ions on the surface of nanocomposites which more ion dissociation promoting a large number of active sites enhancing the adsorption activity. Higher pHs enhance the overall negative charges onto the adsorbent, reflecting on the hydrolysis ability of the metal ions in the solution. Fig. 13 shows Zn(II) adsorption mechanisms on **SiO_2-PYZ** nanocomposite under different pH values.

3.9. The Re-usability of SiO_2-PYZ nanocomposite adsorbent

To investigate the reusability of **SiO_2-PYZ** nanocomposite for the selected heavy metals, the adsorbents' reusability was tested in five successive cycles under similar circumstances, with the adsorbents being reused without further modification from the previous test. After each test, the removal efficiency was calculated, and the data are shown in Fig. 14. After five usages, the **SiO_2-PYZ** nanocomposite's adsorption performance was marginally affected according to the experiments. As a result, the **SiO_2-PYZ** nanocomposite is a stable adsorbent

Table 8 SRB growth bacterial count for **SiO_2 –PYZ** at 40 °C for 28 days.

Compound	Conc. (ppm)	SRB count (cell/ml)	Reduction in SRB count (cell/ml)	Efficiency
Blank	–	10^6	–	–
SiO_2 -PYZ	20	10^2	10^4	66.7%
	40	10^0	10^6	100%

for treating Zn(II) and Cr(III)-laden waters. Overall, the reusability of the **SiO_2-PYZ** nanocomposite supports its potential economic utilization.

3.10. Microbial induced corrosion (MIC)

This research looked into the effectiveness of **SiO_2-PYZ** as a proven antibacterial against SRB microorganisms that induce MIC in anaerobic environments. The methodology for determining **SiO_2-PYZ**'s biocidal activity is based on the NACE standard test method TM0194-14-SG. This common method is used as a routine test in oil and gas wells to measure the rate of microbial growth in places with water anaerobically, such as well trunk lines, and at various phases of processing plants, such as when water is trapped in places like the bottom of oil storage tanks (Bennet, 2017). Fig. 15 compares the number of microbial SRB cells in a water sample taken from an already known contaminated well bed to subsequent dosages of **SiO_2-PYZ** using sets of specially manufactured growth conditions. The inhibitor was diluted in vials in a series of steps. Two series of serial dilutions were examined at different concentrations. The **SiO_2-PYZ** test was done at two doses of 20 and 40 ppm. The antimicrobial activity of **SiO_2-PYZ** against SRB bacteria has been encouraged (Fig. 15). Images were acquired for vial sets injected after a 28-day incubation period, and a blank is shown in Fig. 15. Compared to white vials, the number of black vials (infected vials) was reduced, indicating a biocidal effect.

The data interpretation from the conducted test is shown in Table 8. Because they scored 10^2 cell/ml and 0 cell/ml in the 20 ppm and 40 ppm doses, respectively, it appears that **SiO_2–PYZ** has exhibited the most vigorous action for inhibiting bacterial growth (up to 100%).

4. Conclusions

In this study, **SiO_2-PYZ** nanocomposite adsorbent was synthesized for removal of metal ions from synthetic water and capability against SRB from oilfield water. The best adsorption parameters by the developed nanocomposite were pH 12 and in the presence of 1 gm adsorbent dosage. The linear and nonlinear models of Langmuir, PSO adsorption isotherm, and kinetic models described well the adsorption process. According to the thermodynamic study, adsorption is a spontaneous feasible, and endothermic process. The fact that the negative value of ΔG increases with temperature implies favorable adsorption at low temperatures with a proven physical adsorption mechanism. The **SiO_2-PYZ** nanocomposite can adsorb selected heavy metals in a broad pH range, even in the presence of coexistent ions. It was also demonstrated that the Zn(II) and Cr(III) cationic species are desorbed under alkaline conditions. The **SiO_2-PYZ** nanocomposite could be easily regenerated by giving it the possibility to extend its useful lifetime. Besides, microbial-induced corrosion exhibits good antimicrobial activity against SRB in oil production at two different concentrations, 20 and 40 ppm.

Data availability

Not Applicable.

Funding

There is no funding for the present study.

Author Contribution Statement: All authors have shared writing, revising, and preparing the manuscript.

Declaration of Competing Interest

The authors declare that they have no known competing financial interests or personal relationships that could have appeared to influence the work reported in this paper.

References

Abbas, M.A. et al, 2021. Multifunctional Aspects of the Synthesized Pyrazoline Derivatives for AP1 5L X60 Steel Protection Against MIC and Acidization: Electrochemical, In Silico, and SRB Insights. ACS Omega 6 (13), 8894–8907.

Abdou, M.M. et al, 2013. Synthesis, spectroscopic studies and technical evaluation of novel disazo disperse dyes derived from 3-(2-hydroxyphenyl)-2-pyrazolin-5-ones for dyeing polyester fabrics. Am J Chem 3, 59–67.

Abdou, M.M. et al, 2016. Advancements in tetronic acid chemistry. Part 2: use as a simple precursor to privileged heterocyclic motifs. Mol. Diversity 20 (4), 989–999.

Abdou, M.M., 2017. Utility of 4-hydroxythiocoumarin in organic synthesis. Arabian J. Chem. 10, S3955–S3961.

Abdou, M.M., 2017. 3-Acetyl-4-hydroxycoumarin: Synthesis, reactions and applications. Arabian J. Chem. 10, S3664–S3675.

Abdou, M.M., 2017. Chemistry of 4-Hydroxy-2 (1H)-quinolone. Part 1: Synthesis and reactions. Arabian J. Chem. 10, S3324–S3337.

Abdou, M.M., 2018. Chemistry of 4-hydroxy-2 (1H)-quinolone. Part 2. As synthons in heterocyclic synthesis. Arabian J. Chem. 11 (7), 1061–1071.

Abdou, M.M. et al, 2019. Advancements in tetronic acid chemistry. Part 1: Synthesis and reactions. Arabian J. Chem. 12 (4), 464–475.

Abdou, M.M. et al, 2019. Synthesis and chemical transformations of 3-acetyl-4-hydroxyquinolin-2 (1 H)-one and its N-substituted derivatives: bird's eye view. Res. Chem. Intermed. 45 (3), 919–934.

Abdou, M.M., El-Saeed, R.A., Bondock, S., 2019. Recent advances in 4-hydroxycoumarin chemistry. Part 1: Synthesis and reactions. Arabian J. Chem. 12 (1), 88–121.

Abdou, M.M., El-Saeed, R.A., Bondock, S., 2019. Recent advances in 4-hydroxycoumarin chemistry. Part 2: Scaffolds for heterocycle molecular diversity. Arabian J. Chem. 12 (7), 974–1003.

Aldawsari, A.M. et al, 2020. Activated carbon/MOFs composite: AC/NH_2-MIL-101(Cr), synthesis and application in high performance adsorption of p-nitrophenol. J. Saudi Chem. Soc. 24 (9), 693–703.

Aldawsari, A.M. et al, 2021. Multiuse silicon hybrid polyurea-based polymer for highly effective removal of heavy metal ions from aqueous solution. Int. J. Environ. Sci. Technol. 19 (4), 2925–2938.

Aldawsari, A.M. et al, 2021. Tailoring an efficient nanocomposite of activated carbon-layered double hydroxide for elimination of water-soluble dyes. J. Alloy. Compd. 857, 157551.

Ali, H.M. et al, 2021. Selective and efficient sequestration of Cr(VI) in ground water using trimethyloctadecylammonium bromide impregnated on Artemisia monosperma plant powder. J. Taiwan Inst. Chem. Eng. 125, 122–131.

Bailey, S.E. et al, 1999. A review of potentially low-cost sorbents for heavy metals. Water Res. 33 (11), 2469–2479.

Bakshi, A., Panigrahi, A.K., 2018. A comprehensive review on chromium induced alterations in fresh water fishes. Toxicol. Rep. 5, 440–447.

Barakat, M., 2011. New trends in removing heavy metals from industrial wastewater. Arabian J. Chem. 4 (4), 361–377.

Basu, A. et al, 2019. A study on removal of Cr(III) from aqueous solution using biomass of Cymbopogon flexuosus immobilized in sodium alginate beads and its use as hydrogenation catalyst. J. Taiwan Inst. Chem. Eng. 102, 118–132.

Bennet, D., 2017. Oilfield Microbiology: Effective Evaluation of Biocide Chemicals. In SPE/IATMI Asia Pacific Oil & Gas Conference and Exhibition. OnePetro.

Beveridge, R. et al, 2010. Lung cancer risk associated with occupational exposure to nickel, chromium VI, and cadmium in two population-based case–control studies in Montreal. Am. J. Ind. Med. 53 (5), 476–485.

Chen, G. et al, 2019. Competitive mechanism and influencing factors for the simultaneous removal of Cr (III) and Zn (II) in acidic aqueous solutions using steel slag: Batch and column experiments. J. Cleaner Prod. 230, 69–79.

Da'na, E., 2017. Adsorption of heavy metals on functionalized-mesoporous silica: A review. Microporous Mesoporous Mater. 247, 145–157.

Deng, L. et al, 2017. Fabrication of a novel $NiFe_2O_4$/Zn-Al layered double hydroxide intercalated with EDTA composite and its adsorption behavior for Cr (VI) from aqueous solution. J. Phys. Chem. Solids 104, 79–90.

El-Kemary, M.A. et al, 2018. Sol-gel TiO_2 decorated on eggshell nanocrystal as engineered adsorbents for removal of acid dye. J. Dispersion Sci. Technol. 39 (6), 911–921.

El-Maghrabi, H.H. et al, 2017. Corrigendum: Novel mesoporous silica (MCM-41) and its characterization for oil adsorption from produced water injected in water injection projects using fixed bed column processesbed column processes. Desalin. Water Treat. 60, 70–77.

El-Maghrabi, H.H. et al, 2018. Novel mesoporous silica (MCM-41) and its characterization for oil adsorption from produced water injected in water injection projects using fixed bed column processes (vol 60, 70, 2017). Desalin. Water Treat. 119, 284.

El-Maghrabi, H.H. et al, 2019. Preparation and Characterization of Novel Magnetic $ZnFe_2O_4$–Hydroxyapatite Core-Shell Nanocomposite and Its Use as Fixed Bed Column System for Removal of Oil Residue in Oily Wastewater Samples. Egypt. J. Pet. 28 (2), 137–144.

El-Mahalawy, A.M., Abdou, M.M., Wassel, A.R., 2021. Structural, spectroscopic and electrical investigations of novel organic thin films bearing push-pull azo–Phenol dye for UV photodetection applications. Spectrochim. Acta Part A Mol. Biomol. Spectrosc. 248, 119243.

El-Mahalawy, A.M., Abdou, M.M., Wassel, A.R., 2022. Physical and optoelectronic characteristics of novel low-cost synthesized coumarin dye-based metal-free thin films for light sensing applications. Mater. Sci. Semicond. Process. 137, 106225.

Fathy, M. et al, 2015. Study the adsorption of Ca (II) and Mg (II) on high crosslinked polystyrene divinyl benzene resin. Int. J. Mod. Chem. 7 (1), 36–44.

Fathy, M. et al, 2018. Correction to: Absorption of calcium ions on oxidized graphene sheets and study its dynamic behavior by kinetic and isothermal models. Appl. Nanosci. 8 (8), 2105.

Fu, F., Wang, Q., 2011. Removal of heavy metal ions from wastewaters: a review. J. Environ. Manage. 92 (3), 407–418.

Hao, S. et al, 2016. Optimal synthesis of amino-functionalized mesoporous silicas for the adsorption of heavy metal ions. Microporous Mesoporous Mater. 236, 250–259.

Kausar, A. et al, 2017. Batch versus column modes for the adsorption of radioactive metal onto rice husk waste: conditions optimization through response surface methodology. Water Sci. Technol. 76 (5), 1035–1043.

Kausar, A. et al, 2018. A green approach for the removal of Sr (II) from aqueous media: kinetics, isotherms and thermodynamic studies. J. Mol. Liq. 257, 164–172.

Kong, X.-P., Zhang, B.-H., Wang, J., 2021. Multiple Roles of Mesoporous Silica in Safe Pesticide Application by Nanotechnology: A Review. J. Agric. Food. Chem. 69 (24), 6735–6754.

Lihua, L. et al, 2017. Synthesis of thiol-functionalized mesoporous calcium silicate and its adsorption characteristics for heavy metal ions. J. Environ. Chem. Eng. 5 (6), 6201–6215.

Hosny, R., et al., Utilization of cross-linked chitosan/ACTF biocomposite for softening hard water: optimization by adsorption modeling. Egyptian Journal of Chemistry, 2019. 62(Special Issue (Part 2) Innovation in Chemistry): p. 437-456.

Asif Mahmood, Ahmad Irfan, Jin-Liang Wang, 2021. Developing Efficient Small Molecule Acceptors with sp2-Hybridized Nitrogen at Different Positions by Density Functional Theory Calculations, Molecular Dynamics Simulations and Machine Learning. Chem.—A Eur. J., 28: p. 1-9.

Mahmood, A., Wang, J.-L., 2021. A time and resource efficient machine learning assisted design of non-fullerene small molecule acceptors for P3HT-based organic solar cells and green solvent selection. J. Mater. Chem. A 9, 15684–15695.

Mahmood, A., Irfan, A., Wang, J.-L., 2022. Machine learning and molecular dynamics simulation-assisted evolutionary design and discovery pipeline to screen efficient small molecule acceptors for PTB7-Th-based organic solar cells with over 15% efficiency. J. Mater. Chem. A 10, 4170–4180.

Mahmood, A., Wang, J.-L., 2021. Machine learning for high performance organic solar cells: current scenario and future prospects. Energy Environ. Sci. 14, 90–105.

Massie, K.S., 1980. Chapter 19 Extraction of Inorganic Materials from Sea Water in North-West Europe, in Elsevier Oceanography Series, F.T. Banner, M.B. Collins, and K.S. Massie, Editors. Elsevier. p. 569-572.

Metwally, M. et al, 2012. Synthesis, Structure Investigation and Dyeing Assessment of Novel Bisazo Disperse Dyes Derived from 3-(2'-Hydroxyphenyl)-1-phenyl-2-pyrazolin-5-ones. J. Korean Chem. Soc. 56 (3), 348–356.

Metwally, M. et al, 2012. Synthesis, tautomeric structure, dyeing characteristics, and antimicrobial activity of novel 4-(2-arylazophenyl)-3-(2-hydroxyphenyl)-1-phenyl-2-pyrazolin-5-ones. J. Korean Chem. Soc. 56 (1), 82–91.

Metwally, M.A. et al, 2012. Synthesis, structure elucidation and application of some new azo disperse dyes derived from 4-hydroxycoumarin for dyeing polyester fabrics. Am J Chem 2, 347–354.

Metwally, M.A. et al, 2013. A facile synthesis and tautomeric structure of novel 4-arylhydrazono-3-(2-hydroxyphenyl)-2-pyrazolin-5-ones and their application as disperse dyes. Color. Technol. 129 (6), 418–424.

Mubarak, M.F. et al, 2021. Enhanced Performance of Chitosan via a Novel Quaternary Magnetic Nanocomposite Chitosan/Grafted Halloysitenanotubes@ $Zn\gamma Fe_3O_4$ for Uptake of Cr (III), Fe (III), and Mn (II) from Wastewater. Polymers 13 (16), 2714.

Mubarak, M.F., Hosny, R., 2021. Comparative Analysis on Adsorption Properties and Mechanisms of Nitrate and Phosphate Ions by

a Zn Fe3O4/SiO2 MCM-48 Magnetic Composite: Kinetic and Isotherm Studies. in Water Resources in Arid Lands: Management and Sustainability. Cham: Springer International Publishing.

Naeem, H. et al, 2017. Uranium remediation using modified Vigna radiata waste biomass. Appl. Radiat. Isot. 123, 94–101.

Ortenberg, E., Telsch, B., 2003.Taste and odour problems in potable water. In Handbook of Water and Wastewater Microbiology (pp. 777-793). Academic Press., 2003.

Owlad, M. et al, 2009. Removal of hexavalent chromium-contaminated water and wastewater: a review. Water Air Soil Pollut. 200 (1–4), 59–77.

Ozsoy, H.D., Kumbur, H., 2006. Adsorption of Cu (II) ions on cotton boll. J. Hazard. Mater. 136 (3), 911–916.

Proctor, D.M. et al, 2014. Assessment of the mode of action for hexavalent chromium-induced lung cancer following inhalation exposures. Toxicology 325, 160–179.

Radi, S. et al, 2015. C, N-bipyrazole receptor grafted onto a porous silica surface as a novel adsorbent based polymer hybrid. Talanta 143, 1–6.

Rahman, N. et al, 2021. Efficient removal of Pb (II) from water using silica gel functionalized with thiosalicylic acid: Response surface methodology for optimization. J. King Saud Univ.-Sci. 33, (1) 101232.

Rahman, N., Haseen, U., 2014. Equilibrium modeling, kinetic, and thermodynamic studies on adsorption of Pb (II) by a hybrid inorganic–organic material: polyacrylamide zirconium (IV) iodate. Ind. Eng. Chem. Res. 53 (19), 8198–8207.

Rahman, N., Varshney, P., 2020. Assessment of ampicillin removal efficiency from aqueous solution by polydopamine/zirconium (IV) iodate: optimization by response surface methodology. RSC Adv. 10 (34), 20322–20337.

Rahman, N., Varshney, P., 2021. Effective removal of doxycycline from aqueous solution using CuO nanoparticles decorated poly (2-acrylamido-2-methyl-1-propanesulfonic acid)/chitosan. Environ. Sci. Pollut. Res. 28 (32), 43599–43617.

Rahman, N., Khan, M.F., Nasir, M., 2020. Experimental design approach for optimization of Pb (II) removal from aqueous solution using poly-o-toluidine/stannic (IV) triethanolamine as adsorbent. Environ. Technol. Innovation 17, 100634.

Rahman, N., Khan, M.F., Nasir, M., 2020. Experimental design approach for optimization of Pb(II) removal from aqueous solution using poly-o-toluidine/stannic(IV) triethanolamine as adsorbent. Environ. Technol. Innovation 17, 100634.

Rahman, N., Nasir, M., 2020. Facile synthesis of thiosalicylic acid functionalized silica gel for effective removal of Cr (III): Equilibrium modeling, kinetic and thermodynamic studies. Environ. Nanotechnol. Monit. Manage. 14, 100353.

Rahman, N., Varshney, P., 2021. Facile synthesis and characterization of Zn (II)-impregnated chitosan/graphene oxide: evaluation of its efficiency for removal of ciprofloxacin from aqueous solution. J. Inorg. Organomet. Polym Mater. 31 (8), 3595–3612.

Shoueir, K.R. et al, 2016. Adsorption studies of Cu^{2+} onto poly (vinyl alcohol)/poly (acrylamide-co-N-isopropylacrylamide) core–shell nanogels synthesized through surfactant-free emulsion polymerization. Sep. Sci. Technol. 51 (10), 1605–1617.

Shoueir, K.R. et al, 2016. Macrogel and nanogel networks based on crosslinked poly (vinyl alcohol) for adsorption of methylene blue from aqua system. Environ. Nanotechnol. Monit. Manage. 5, 62–73.

Shoueir, K.R. et al, 2017. Synthesis of monodisperse core shell PVA@P (AMPS-co-NIPAm) nanogels structured for pre-concentration of Fe (III) ions. Environ. Technol. 38 (8), 967–978.

Shoueir, K.R., 2020. Green microwave synthesis of functionalized chitosan with robust adsorption capacities for Cr (VI) and/or RHB in complex aqueous solutions. Environ. Sci. Pollut. Res. 27 (26), 33020–33031.

Silva, S. et al, 2020. Cracking mechanism in API 5L X65 steel in a CO_2-saturated environment–Part II: A study under cathodic polarisation. Eng. Fail. Anal. 113, 104550.

Slowing, I., Trewyn, B.G., Lin, V.-S.-Y., 2006. Effect of surface functionalization of MCM-41-type mesoporous silica nanoparticles on the endocytosis by human cancer cells. J. Am. Chem. Soc. 128 (46), 14792–14793.

Sun, D., Wu, M., Xie, F., 2018. Effect of sulfate-reducing bacteria and cathodic potential on stress corrosion cracking of X70 steel in sea-mud simulated solution. Mater. Sci. Eng., A 721, 135–144.

Toor, S.K., Kushwaha, J.P., Sangal, V.K., 2019. Single and Binary Adsorption of Zn (II) and Cr (VI) Heavy Metals onto Synthesized Silica-Based MCM-41. ChemistrySelect 4 (9), 2576–2584.

Üçer, A., Uyanik, A., Aygün, Ş., 2006. Adsorption of Cu (II), Cd (II), Zn (II), Mn (II) and Fe (III) ions by tannic acid immobilised activated carbon. Sep. Purif. Technol. 47 (3), 113–118.

Vardhan, K.H., Kumar, P.S., Panda, R.C., 2019. A review on heavy metal pollution, toxicity and remedial measures: Current trends and future perspectives. J. Mol. Liq. 290, 111197.

Wakai, S., 2020. Electron Flow Rate in Microbiologically Influenced Corrosion and Its Applications. In: Electron-Based Bioscience and Biotechnology. Springer, pp. 193–205.

Wakai, S., et al., 2018. Microbial Corrosion Induced by Co-Existence of Acetobacterium Sp. and Desulfovibrio Sp. Enriched from Bottom Water in Oil-Storage Tank. EUROCORR.

Wamba, A.G. et al, 2018. Grafting of Amine functional group on silicate based material as adsorbent for water purification: a short review. J. Environ. Chem. Eng. 6 (2), 3192–3203.

Wang, Y. et al, 2017. Carcinogenicity of chromium and chemoprevention: a brief update. OncoTargets and therapy 10, 4065.

Wang, X.-N., Gu, Y.-G., Wang, Z.-H., 2022. Rare earth elements in different trophic level marine wild fish species. Environ. Pollut. 292, 118346.

Yalçın, M.S. et al, 2020. Phallus impudicus loaded with γ-Fe_2O_3 as solid phase bioextractor for the preconcentrations of Zn (II) and Cr (III) from water and food samples. Process Biochem. 92, 149–155.